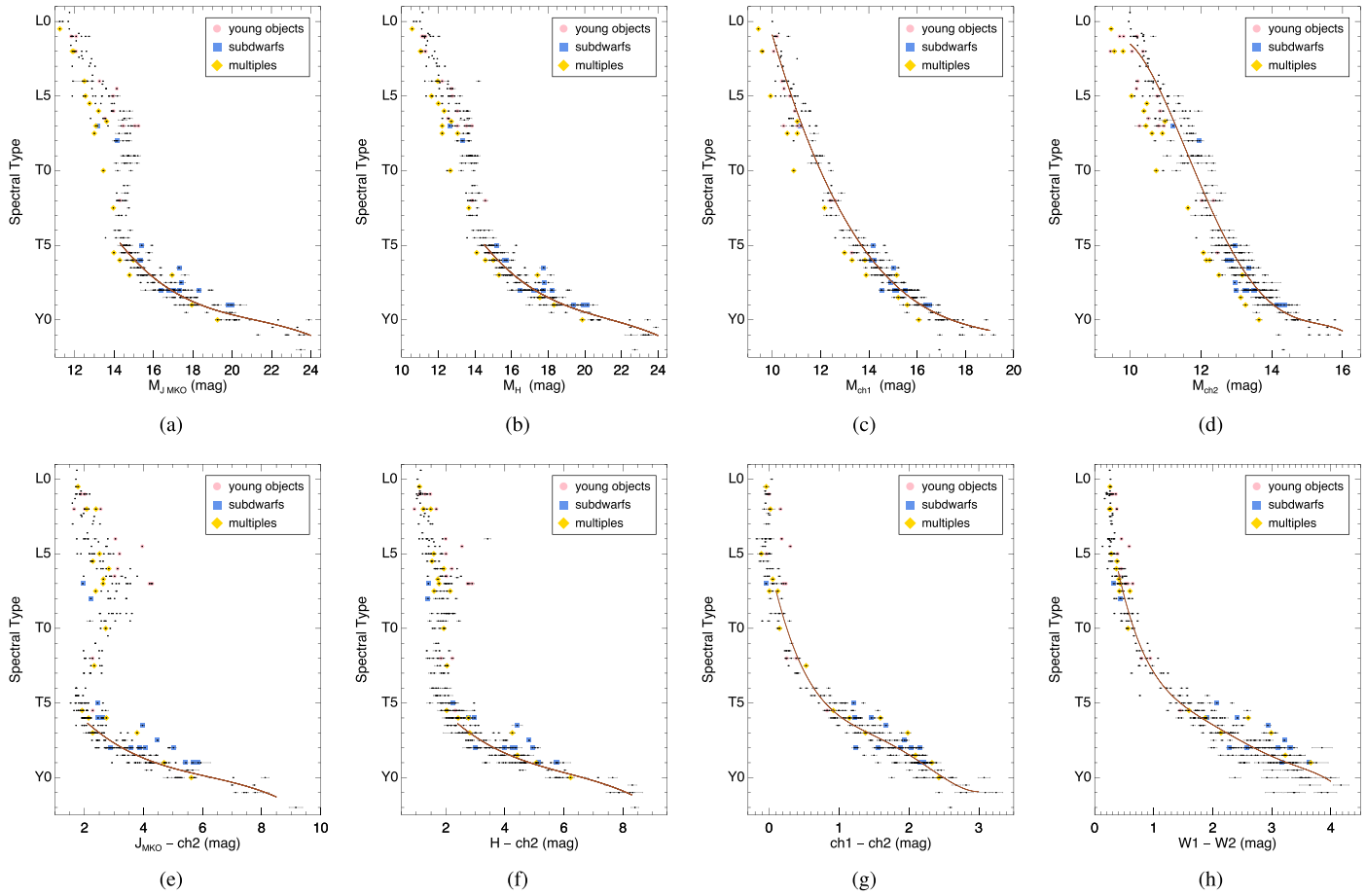

Figure 17. Plots identical to those of Figure 16, except that the *x*- and *y*-axes have been reversed. Polynomial fits to provide a translation from absolute magnitude or color into spectral type are shown in brown and described in Table 13. These fits exclude known young objects (pink circles, Section 7.1), subdwarfs (blue squares, Section 7.2), and multiple systems (yellow diamonds, Section 7.3).

predict low-metallicity objects to fall. We consider this to be a normal Y dwarf in subsequent analysis, pending the empirical spectroscopic identification of other Y subdwarfs.

3. WISE 0430+4633: This T8 dwarf falls along the locus of subdwarfs in the color-type plots of Figures 16(e) and (f). It is also a color outlier on the color-type plot of Figure 16(h) and the color–color plot of Figure 18(f). The spectral classification of this object is based on only a *J*-band spectrum by Mace et al. (2013a). As with WISE 0316+4307 above, a spectrum across the full *JHK* wavelength range is needed to confirm whether a subdwarf classification is warranted.
4. UGPS 0521+3640: This T8.5 dwarf falls along the subdwarf locus in the absolute magnitude-color plot of Figure 18(b). It is also an outlier on the color–color plot of Figure 18(f). However, this source's photometry may be confused by the halo of a much brighter star. The near-infrared spectrum by Burningham et al. (2011) shows no peculiarities, so we think it is only the poor photometry that is causing this object to appear as an outlier.
5. WISE 0751−7634: This T9 dwarf falls along the subdwarf locus in the absolute magnitude-color plots of Figures 18(a), (b) and 19(a), (b), as well as in the color–color plot of Figure 19(e). It is also an outlier on the color–color plot of Figure 19(f). The near-infrared spectrum shown by Kirkpatrick et al. (2011) has low S/N in the *K* band and may show the flux suppression typical of T subdwarfs, but an improved spectrum is needed to verify this. Leggett et al. (2017) notes that this object falls within the locus on the $J-\mathrm{ch2}$ versus $\mathrm{ch1}-\mathrm{ch2}$ diagram where substellar models predict low-metallicity objects to fall. We await improved spectroscopic data before classifying this object as a subdwarf.
6. WISE 1112−3857: This T9 dwarf falls along the subdwarf locus in the color-type plots of Figure 16(e), (f), and the color–color plot of Figure 18(d). The near-infrared spectrum presented in Tinney et al. (2018) does not extend to the *K*-band but appears to show excess flux on the blueward side of *Y*-band, as seen in other T subdwarfs (see Section 7.2). A more complete spectrum at higher S/N is needed to confirm the subdwarf hypothesis.
7. WISE 1141−3326: This is a Y0 dwarf that falls along the subdwarf locus in the absolute magnitude-color plots of Figures 18(a) and 19(a), and the color–color plots of Figures 18(d) and 19(e). As noted in Kirkpatrick et al. (2019a), however, these anomalies can likely be attributed to photometric contamination at earlier epochs when the source was passing in front of a background galaxy.

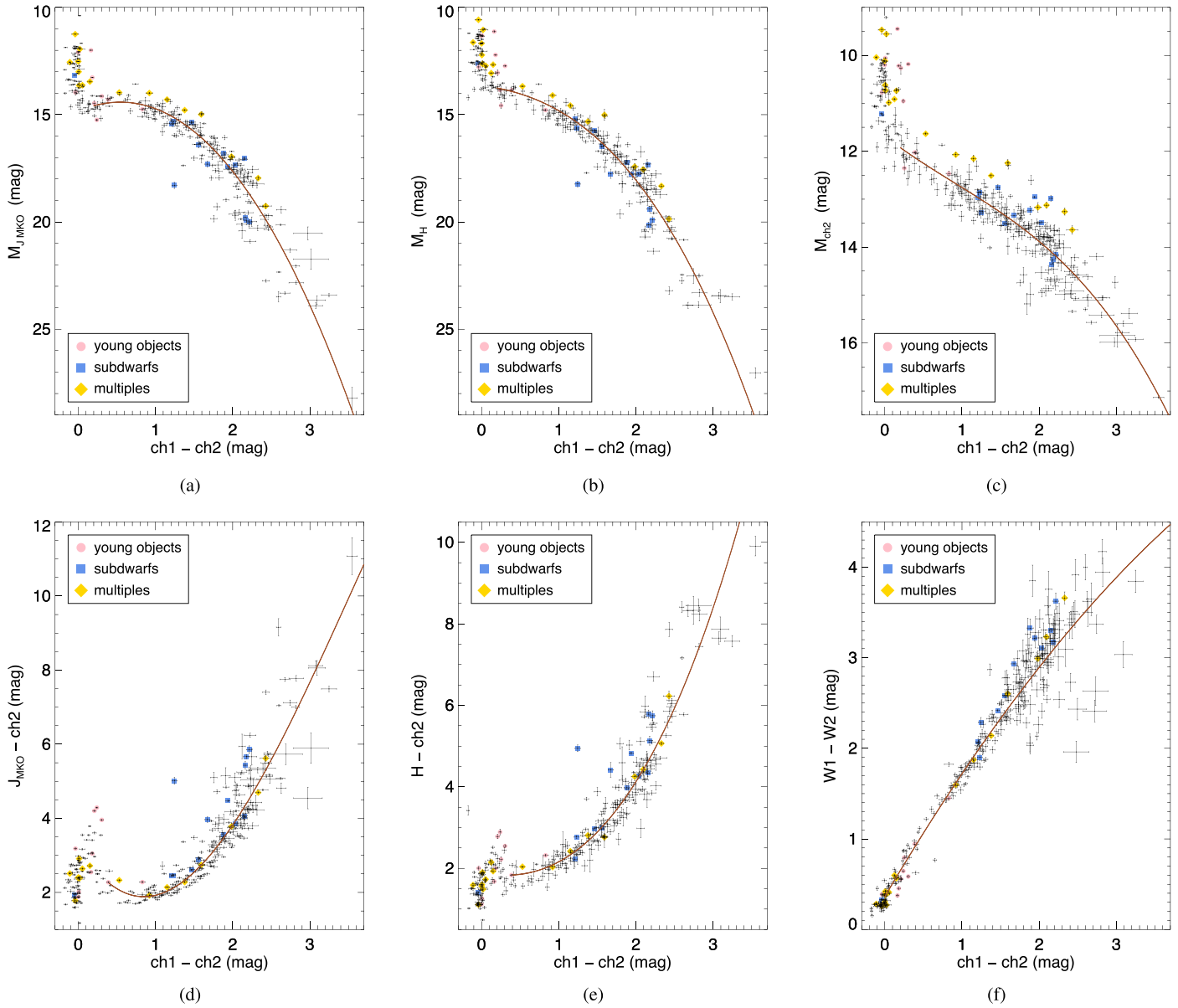

Figure 18. Plots of various absolute magnitudes (a)–(c) and colors (d)–(f) as a function of ch1 − ch2 color. Only members of the 20 pc census are shown, and plots (a)–(c) show only the subset of 20 pc objects having parallaxes measured to better than 12.5%. Polynomial fits that exclude known young objects (pink circles, Section 7.1), subdwarfs (blue squares, Section 7.2), and multiple systems (yellow diamonds, Section 7.3) are shown in brown and described in Table 13. Fits include only those points with ch1 − ch2 > 0.2 mag for panels (a)–(e).

8. WISE 1818−4701: A spectrum of this object has not yet been acquired, but it is believed to be a late-T dwarf. It falls along the subdwarf locus in the absolute magnitude-color plot of Figure 19(a) and color–color plot of Figure 19(e). A spectrum is required to confirm or refute the subdwarf hypothesis.
9. GJ 836.7B (2144+1446): This T3 dwarf, also known as HN Peg B, appears along the subdwarf sequence in the color–color plot of Figure 19(f) and is an outlier on the color-type plot of Figure 16(h) and the color–color plot of Figure 18(f). Luhman et al. (2007) cite an age of ∼300 Myr for the system, and Valenti & Fischer (2005) find that the primary has [M/H] ≈ −0.01. Since this object is obviously not a subdwarf, we suspect that the CatWISE2020 photometry may be corrupted due to the proximity of the bright primary itself. The AllWISE and CatWISE2020 photometry (Table A1) differ in both W1 and W2 by $> 5\sigma$, indicating that the the automated measurements are likely poor. Further evidence that the W1 − W2 color may be suspect is the fact that similar plots with ch1 − ch2 color (Figures 16(g) and 18(e)) show this source falling along the locus of normal field dwarfs.
10. GJ 1263B (2146−0010): This T8.5 dwarf, also known as Wolf 940B, lies along the subdwarf locus in Figures 19(a), (b). Burningham et al. (2009) find that the primary has an age of ∼3.5 Gyr and metallicity of [Fe/H] = −0.06 ± 0.20, so the B component cannot be a subdwarf. As with GJ 836.7B, the AllWISE and CatWISE2020 photometry (Table A1) differ in both

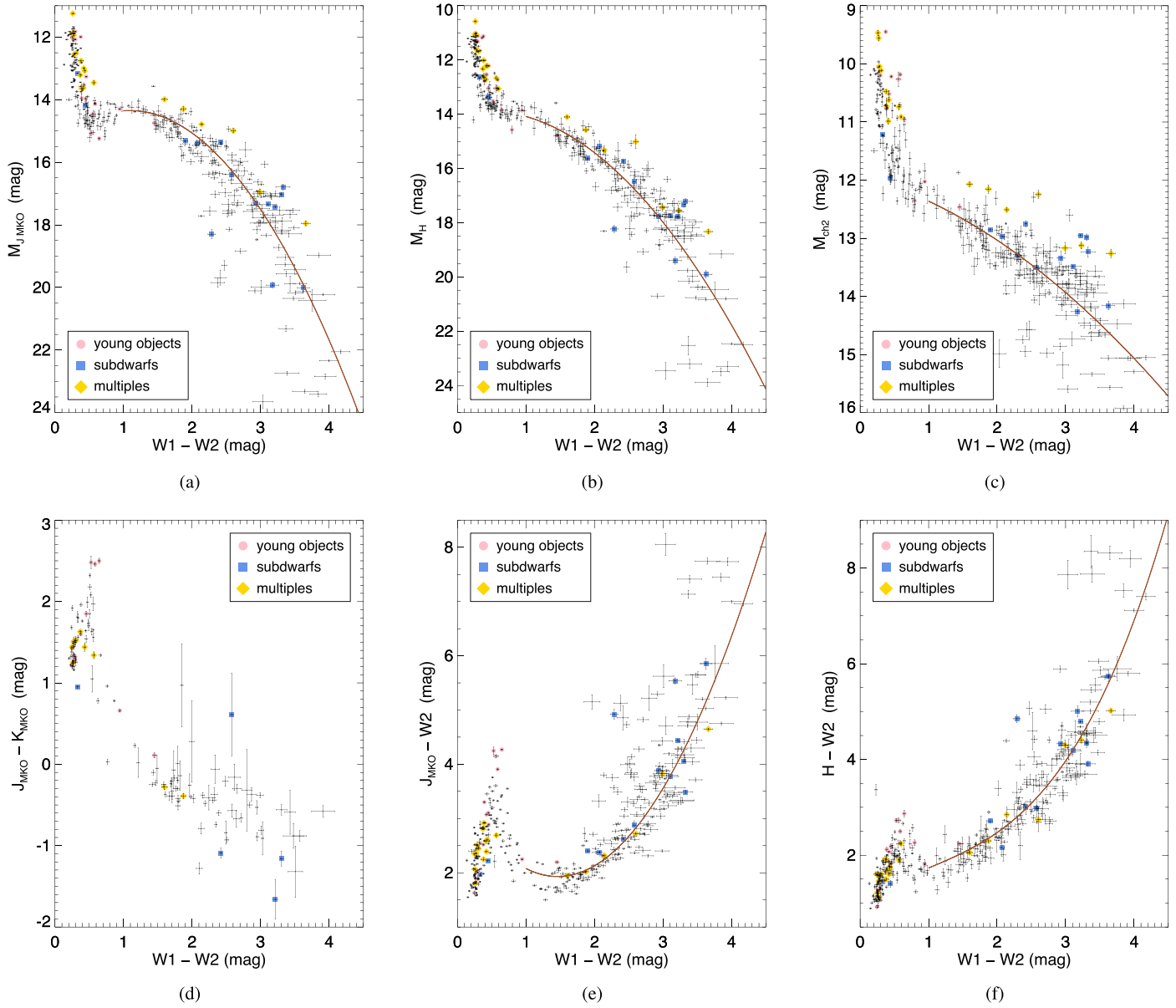

Figure 19. Plots of various absolute magnitudes (a)–(c) and colors (d)–(f) as a function of W1 − W2 color. Only members of the 20 pc census are shown, and plots (a)–(c) show only the subset of 20 pc objects having parallaxes measured to better than 12.5%. Polynomial fits that exclude known young objects (pink circles, Section 7.1), subdwarfs (blue squares, Section 7.2), and multiple systems (yellow diamonds, Section 7.3) are shown in brown and described in Table 13. In panels (a)–(c), the fits include only those points with W1 − W2 > 1.0 mag, and in panels (e) and (f), the fits include only those points with W1 − W2 > 0.8 mag.

W1 and W2, in this case by $> 10\sigma$ and $> 6\sigma$, respectively. Further evidence that the W1 − W2 color may be suspect is the fact that similar plots with ch1 − ch2 color (Figures 18(a), (b)) show this source to fall along the normal locus. We suspect that the bright primary has corrupted the WISE photometry of the secondary.

7.7. Potential Multiples

Several L, T, and Y dwarfs within the 20 pc census have been previously published as suspected multiples and either remain unconfirmed or have subsequently been discounted. Several others are newly addressed here as suspected binary systems. Suspected companions are denoted by brackets ("[B]" or "[C]") around the suffix both in the text below and in Table 11.

1. WISE 0309−5016A[B]: This T7 dwarf is an outlier on the absolute magnitude-type plot of Figure 16(d) and on the absolute magnitude-color plots of Figures 18(b), (c); 19(a)–(c); 20(a)–(c); and 21(a)–(c). The consistent overluminosity of this object across colors and bands strongly points to its being an unresolved double with components of near-equal magnitude. As we did in Kirkpatrick et al. (2019a), we consider it to be a two-body system in subsequent analysis.
2. WISE 0350−5658: This Y1 dwarf falls well above the mean trend in Figure 18(b). Oddities in absolute magnitude-type plots were also noted in Kirkpatrick et al. (2019a). Few Y1 dwarfs are presently known, so it is unclear to what extent this is just cosmic scatter for normal dwarfs of this spectral type. We consider this object to be single.

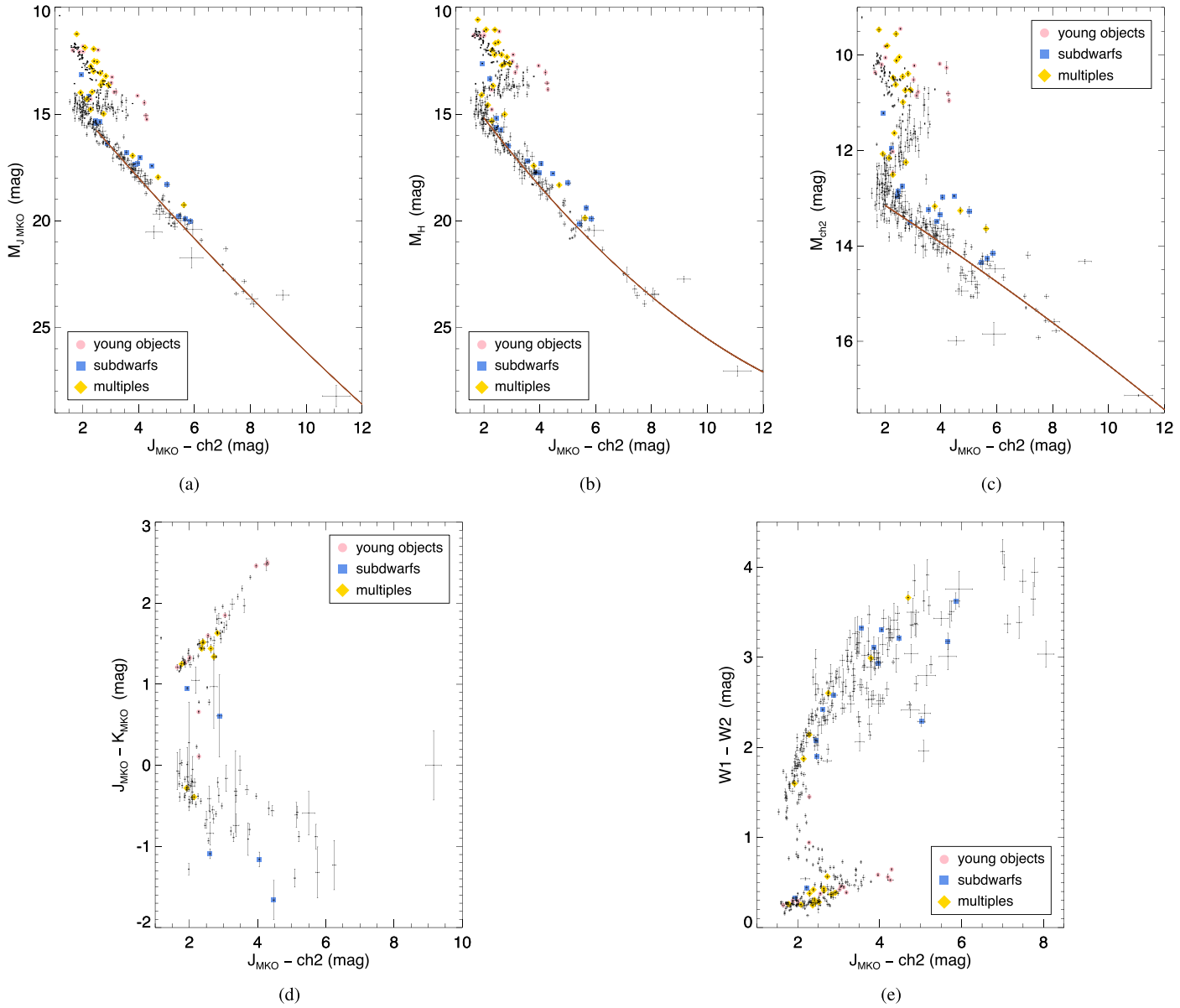

Figure 20. Plots of various absolute magnitudes (a)–(c) and colors (d)–(e) as a function of $J_{\rm MKO}$ − ch2 color. Only members of the 20 pc census are shown, and plots (a)–(c) show only the subset of 20 pc objects having parallaxes measured to better than 12.5%. All five panels are supplemented with W2 magnitudes when ch2 is not available, as described in Section 7.4. Polynomial fits that exclude known young objects (pink circles, Section 7.1), subdwarfs (blue squares, Section 7.2), and multiple systems (yellow diamonds, Section 7.3) are shown in brown and described in Table 13. These fits are restricted to points with $M_{J\rm MKO} \geqslant 16.0$ mag in panel (a), $M_H \geqslant 15.0$ mag in panel (b), and $M_{\rm ch2} \geqslant 13.0$ mag in panel (c).

3. WISE 0535−7500: This ⩾Y1: dwarf falls well above the mean trend on the absolute magnitude-type plot of Figure 16(d) and on the absolute magnitude-color plots of Figures 18(c); 20(a), (c); and 21(a)–(c). This overluminosity was also noted by Tinney et al. (2014); Leggett et al. (2017), and Kirkpatrick et al. (2019a). Opitz et al. (2016) used adaptive-optics imaging to rule any equal-magnitude companion at a separation greater than ∼1.9 au. As with WISE 0350−5658 above, it is unclear to what extent this may just be cosmic scatter for normal dwarfs of this spectral type, since few are known. We consider this object to be single.
4. WISE 0546−0959: This T5 dwarf falls above the mean locus on the M_H versus ch1 − ch2 diagram of Figure 18(b) and the M_H versus W1 − W2 diagram of Figure 19(b). Because it appears overluminous only in the H band, we consider this object to be single.
5. 2MASS 0559−1404: This mid-T dwarf falls well above the mean locus on all of the plots based on absolute magnitude in Figures 16, 18, and 19. It is also an outlier on the $M_{J\rm MKO}$ versus $J_{\rm MKO}$ − ch2 plot of Figure 20(a). Two hypotheses have been proposed to explain the overluminosity, which was first noted by Dahn et al. (2002): (1) Burgasser (2001) suggested that the object was an equal-magnitude binary. (2) Burgasser et al. (2003c) later proposed that the quick dissipation of clouds near the L-to-T dwarf transition could be responsible for the overluminosity, which is largest in the J band. However, both of these hypotheses have encountered problems in the intervening years. The cloud

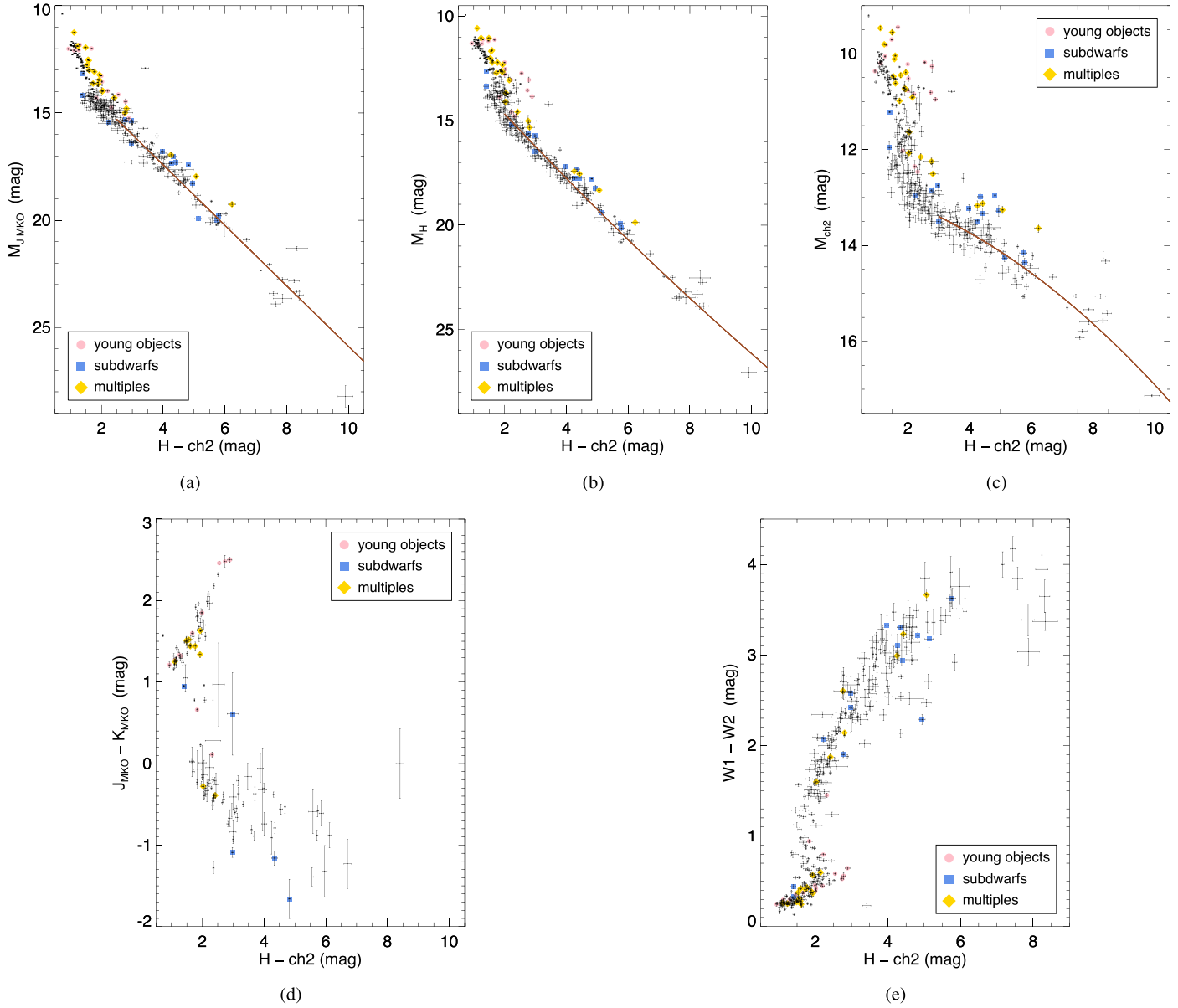

Figure 21. Plots of various absolute magnitudes (a)–(c) and colors (d)–(e) as a function of $H - \mathrm{ch2}$ color. Only members of the 20 pc census are shown, and plots (a)–(c) show only the subset of 20 pc objects having parallaxes measured to better than 12.5%. All five panels are supplemented with W2 magnitudes when ch2 is not available, as described in Section 7.4. Polynomial fits that exclude known young objects (pink circles, Section 7.1), subdwarfs (blue squares, Section 7.2), and multiple systems (yellow diamonds, Section 7.3) are shown in brown and described in Table 13. These fits are restricted to points with $M_{J\mathrm{MKO}} \geqslant 16.0$ mag in panel (a), $M_H \geqslant 15.0$ mag in panel (b), and $M_{\mathrm{ch2}} \geqslant 13.0$ mag in panel (c).

disruption theory was largely invoked to explain the *J*-band overluminosity (Tsuji & Nakajima 2003), but as our figures show, this overluminosity is present across all bands from *J* through W2. The binary theory has yet to be confirmed, either. High-resolution HST imaging by Burgasser et al. (2003c) showed no indication of a hidden companion down to a separation of 0.″09. Using radial velocity measurements covering a 4.4 yr period, Zapatero Osorio et al. (2007) found no velocity variations (to $1\sigma = 0.5$ km s^{-1}). Other radial velocity measurements by Prato et al. (2015) were able to rule out a companion with a period of a day or less, but these authors stress that there is still orbital parameter space between their sampled region and the 0.″09 (0.9 au) limit of the HST imaging mentioned above. Given the inability of observers to confirm the binary hypothesis for this object, we will assume the object is a single dwarf in subsequent analysis.

6. PSO 0652+4127: Best et al. (2013) label this object as a possible binary based on the fact that some near-infrared spectral indices better match a L8+T2.5 composite than the single T0 type. Their single-object photometric distance suggests the object falls at 14.2 ± 1.2 pc, whereas the binary hypothesis suggests 20.1 ± 2.4 pc. Our Spitzer parallax gives a distance of 17.4 ± 1.0 pc, which is intermediate between the two estimates. In the absence of data confirming a companion, we consider this object to be single.
7. SDSS 0758+3247: This early T dwarf was discovered by Knapp et al. (2004). It was identified by Burgasser et al. (2010b) as a weak candidate for unresolved binarity due to its near-infrared spectral morphology. However, as

stated in that paper, the single-object spectral fit outperformed that of the best binary fit. Nonetheless, the spectral type listed in the SIMBAD database shows this as a composite type. Bardalez Gagliuffi et al. (2015) list this system as a "visual spectral binary" but surmise that it is comprised of two components with types of T2.2 ± 0.0 and T2.3 ± 0.0, despite the fact that it is not possible to detect a binary comprised of identical components using low-resolution spectral morphology alone. Our plot of M_H versus near-infrared spectral type, for example, shows no overluminosity of this object compared to other early-T dwarfs, ruling out the equal-magnitude binary hypothesis. We thus consider this object to be a single brown dwarf.

8. SDSS 0857+5708: This L8 dwarf falls above the mean trend on the plots of M_{ch1} and M_{ch2} versus spectral type in Figures 16(c), (d). Given that there is no evidence of overluminosity in other diagrams and that there is no indication in the literature of binarity, we consider this to be a single object.
9. WISE 0920+4538: Given that this L9 dwarf is labeled only as a weak binary candidate in Mace et al. (2013a) and that some of its peculiarities may be attributed to spectroscopic variations (Best et al. 2013), we consider this to be a single object.
10. 2MASS 0939−2448A[B]: This T8 dwarf has been considered an unresolved, equal-magnitude binary for many years based on its overluminosity, as discussed in Kirkpatrick et al. (2019a). In Section 7.2, we noted that the spectrum shows signs of low metallicity as well. Thus, we consider this to be a T subdwarf binary.
11. PSO 0956−1447: Best et al. (2015) list this late-L dwarf as a marginal spectral binary candidate. In the absence of any confirmation via high-resolution imaging, we consider this to be a single object.
12. SDSS 1048+0111: This early- to mid-L dwarf falls above the mean locus on the plots of absolute magnitude versus spectral type in Figure 16(a), (b). Reid et al. (2006a) did not find any evidence of binarity in high-resolution HST imaging. Furthermore, we note that our perceived overluminosity vanishes if we plot against the optical spectral type of L1 instead of the near-infrared type of L4 (Table 11). We consider this to be a single object.
13. 2MASS 1231+0847: This T5.5 dwarf is overluminous for its ch1 − ch2 and W1 − W2 color on Figures 18(a)–(c) and 19(a)–(c). The object was observed with high-resolution imaging on HST by Aberasturi et al. (2014), who found no companion with a separation $> 0\farcs3$ down to $\Delta J \approx 2.5$ mag (their Figure 7). As discussed in Kirkpatrick et al. (2019a), Burgasser et al. (2004) proposed that this object's broad K I lines might indicate a higher gravity that is the consequence of lower metallicity. Given the uncertain cause of this object's peculiarities, we will consider it to be a single dwarf of normal metallicity in subsequent analysis.
14. WISE 1318−1758: This T8 dwarf is overluminous on the M_H versus ch1 − ch2 plot of Figure 18(b) and the M_H versus J_{MKO} − ch2 plot of Figure 20(b). Because the object does not appear overluminous on other plots, we consider it to be single.
15. WISE 1322−2340: This late-T dwarf is overluminous only on the M_H versus ch1 − ch2 plot of Figure 18(b), although Kirkpatrick et al. (2019a) noted it was an outlier in H − ch2 color as well. However, the object does not distinguish itself on other plots, and Gelino et al. (2011) ruled out any companion with a separation $> 0\farcs2$ down to $\Delta H \approx 4.0$ mag. We consider this object to be single.
16. ULAS 1416+1348: In Kirkpatrick et al. (2019a), we considered this (sd)T7.5 to be an unresolved double based on its overluminosity with respect to normal late-T dwarfs and with respect to the few sdT dwarfs identified in that paper. However, it now appears that overluminosity with respect to normal T dwarfs of the same color or spectral type is a trait shared with a wider variety of low-metallicity T dwarfs. We therefore now consider this to be a single object.
17. WISE 1627+3255A[B]: This mid-T dwarf is overluminous on the absolute magnitude-color plots of Figures 18(a)–(c) and 19(a)–(c). Although Gelino et al. (2011) found no companion down to $\Delta H \approx 5$ mag at separations $> 0\farcs2$, we consider this object to nonetheless be a tight unresolved binary, just as Kirkpatrick et al. (2019a) concluded.
18. DENIS 1705−0516: Kendall et al. (2004) discovered this early-L dwarf. Reid et al. (2006a), using HST/NICMOS imaging in 2005 Jun, found a faint source separated by $1\farcs36$ and consistent with either a distant (1–2 kpc), unrelated mid-M dwarf or a physically related early-T dwarf. Our analysis of more recent imaging by HST/WFC3 (Program 13724; PI: T. Henry) as well as J and K_S imaging by VHS show that the putative companion is a stationary background source, the motion of the early-L dwarf having increased the separation between the two objects to $2\farcs9$ arcsec by 2015 Mar. We consider this L dwarf to be a single object.
19. WISE 1804+3117: This late-T dwarf is overluminous only on the M_{ch1} versus spectral type diagram of Figure 16(c). This object has both an uncertain type of T9.5: and falls close to the Y dwarf regime where the identification of binarity has proven to be problematic. Therefore, as Kirkpatrick et al. (2019a) also concluded, we will consider this object to be single in our subsequent analysis.
20. Gaia 1831−0732: This object does not yet have a measured spectral type, but if a classification of L0 is verified, it is overluminous relative to other L0 dwarfs on the absolute magnitude versus type plots of Figures 16(a)–(d). It is also overluminous on the absolute magnitude versus color plots of Figures 18(a)–(c), but this overluminosity would vanish if the object were actually a late-M dwarf. The fact that it is an outlier on the color–color plot of Figure 18(e) strongly suggests that it is, indeed, an M dwarf. Given the evidence that this object is earlier than L0, we exclude it from subsequent analyses.
21. Gl 758B (1923+3313): This late-T dwarf companion was discovered using Subaru/HiCIAO by Thalmann et al. (2009), who also reported a possible third member of the system. Using the same instrument, Janson et al. (2011) confirmed that this purported Gl 758 "C" was a background star based on data with a ∼1.5 yr baseline.
22. 2MASS 2126+7617A[B]: This object appears overluminous on Figure 16(b). Kirkpatrick et al. (2010) note

that this object has peculiar spectra in both the optical and near-infrared, and the spectral types are discrepant between the two—L7 in the optical, and T0 pec in the near-infrared. These authors also found that a spectral binary comprised of an L7 dwarf and a T3.5 dwarf accounts for the main peculiarities in the near-infrared spectrum. Given that this is a strong case for a spectral binary, we tentatively include the B component in our subsequent analysis.

23. 2MASS 2139+0220: This early-T dwarf was identified as a possible unresolved binary based on its near-infrared spectral morphology by Burgasser et al. (2010b). Individual components of types L8.5 and T3.5 were suggested, although it was noted that the synthetic composite type still failed to reproduce important features in the observed spectrum. This object is now noted for its extreme variability (26% in the *J* band), leading Radigan et al. (2012) to conclude that the object's variations were caused either by multilayered clouds or a cloud layer with holes. Bardalez Gagliuffi et al. (2015) conjecture that some candidate spectral binaries may instead be single objects whose photospheres are comprised of multi-component cloud layers of differing temperatures. We consider 2MASS 2139+0220 to be a single object.

7.8. Other Outliers

1. SDSS 0000+2554: This T4.5 dwarf is an outlier on the W1 − W2 versus spectral type plot of Figure 16(h), the W1 − W2 versus ch1 − ch2 plot of Figure 18(f), and the $J_{\rm MKO} - K_{\rm MKO}$ versus W1 − W2 plot of Figure 19(d). Examination of the WISE images shows this object to be buried within the halo of the bright star Z Pegasi, which must be corrupting the WISE colors.
2. WISE 0715−1145: This object appears as a color outlier on at least nine of the previous plots (Figures 16(b), (f); 18(e); 19(b), (f); 21(a), (b), (c), (e)) but does not fall in the locus of known young objects, subdwarfs, or unresolved multiples. It is an L4 pec (blue) dwarf whose near-infrared spectrum is much bluer than the standard L4 dwarf but lacks indications of low metallicity (Kirkpatrick et al. 2014), and it is one of just six blue L dwarfs known in the 20 pc census—the others being SIPS J0921−2104, 2MASS 1300+1912, 2MASS 1721+3344, VVV 1726−2738, and WISE 2141−5118. Only three of these others (2MASS 1300+1912, 2MASS 1721+3344, and VVV 1726−2738) appear as outliers on the previous plots, and these distinguish themselves only in Figure 16, which is based on spectral type. WISE 0715−1145 therefore appears to be the most extreme color outlier of the 20 pc blue L dwarfs. Faherty et al. (2009) noted that the general population of blue L dwarfs, despite not showing obvious signs of low metallicity, nonetheless have kinematics consistent with an old age.
3. WISE 1828+2650: This Y dwarf is overluminous on Figures 16(a)–(d); 20(b), (c); and 21(b), (c). It also falls along the subdwarf locus in Figure 18(d). This object was discussed in Section 8.2.47 of Kirkpatrick et al. (2019a). Compared to all other Y dwarfs with near-infrared spectra, this object has a unique spectrum that does not compare well with the known suite of theoretical models (M. C. Cushing et al. 2020, in preparation).

8. Temperatures and Space Densities

8.1. Assigning Each Object to a T_{eff} Bin

Finding the functional form of the mass function from our 20 pc census is not a straightforward exercise, because mass is not an observable quantity. Moreover, because most of the objects in our L, T, and Y dwarf census are brown dwarfs, they continue to cool as they age, and as a result there is no direct mapping from spectral type to mass unless the age of the object is known. Only a small number of the objects within the census have age estimates—i.e., confirmed members of young moving groups and companions to higher-mass stars whose ages are known through other means.

Because the bulk of our objects have no age estimates, we rely instead on simulating empirical distributions using various assumed forms of the mass function, an assumed star formation rate over the interval of interest, and theoretical models to evolve each object to the current epoch. This work is described in detail in Sections 9.1 and 9.2 of Kirkpatrick et al. (2019a). The evolutionary models allow us to transform the predictions into distributions of either effective temperature or bolometric luminosity. Both of these quantities have their own limitations, however. Effective temperature is not a directly observable quantity: it requires either forward modeling (comparison to atmospheric models), inverse modeling ("retrieval" analysis), or calculation via the Stefan–Boltzmann Law. Measuring effective temperature via the Stefan–Boltzmann equation would require only a measurement of the bolometric luminosity and an assumption about the object's radius; fortunately, for most of these old brown dwarfs, the radius can be assumed to be $\sim 1 R_{\rm Jup}$, due to their electron degeneracy. However, if bolometric luminosities were already measured, we could forgo temperature determinations entirely and simply compare our observed luminosity distributions to the simulations. At present, however, we have insufficient data with which to compute accurate bolometric luminosities for most of these objects, although more complete spectral coverage over the bulk of these objects' spectral energy distribution will soon be obtainable using the Spectro-Photometer for the History of the Universe, Epoch of Reionization and Ices Explorer (SPHEREx; Doré et al. 2016, 2018), supplemented at longer wavelengths with data from WISE and the James Webb Space Telescope (Gardner et al. 2006).

For now, we are left to convert our sample into a distribution of effective temperature. Filippazzo et al. (2015) calculated bolometric luminosities for a large number of late-M, L, and T dwarfs, and used those to compute effective temperatures once a radius was deduced from model calculations. (These radii were very close to $\sim 1 R_{\rm Jup}$, as expected, given that most of these objects are old brown dwarfs that have contracted to their final equilibrium radius.) Those authors then plotted various observable parameters against the resulting effective temperature measurements and found that the relation with the smallest scatter was $T_{\rm eff}$ versus M_H. For objects in our 20 pc sample that are thought to be old field objects, we can therefore use M_H to transform into $T_{\rm eff}$. However, a few objects do not have *H*-band measurements, and for those, we can use the measured spectral type (or its estimate) as the arbiter of effective temperature.

The relations presented in Filippazzo et al. (2015) predate the release of Gaia DR2 and do not extend into the Y dwarf regime. Therefore, we have updated the data presented in that

Table 14
Late-M, L, T, and Y Dwarfs with $T_{\rm eff}$ Measurements

Name[a]	SpT[b]	$\varpi_{\rm abs}$ (mas)	$T_{\rm eff}$ (K)	H (mag)	Ref[c]
(1)	(2)	(3)	(4)	(5)	(6)
SDSS 0000+2554	14.5	70.8 ± 1.9	1227 ± 95	14.731 ± 0.074	TTFT
2MASS J00034227-2822410	−2.5	24.351 ± 0.201	2871 ± 76	12.376 ± 0.028	FGFF
BRI B0021-0214	−0.5	79.965 ± 0.221	2390 ± 80	11.084 ± 0.022	FGFF
2MASS 0034+0523	16.5	118.8 ± 2.7	899 ± 82	15.58 ± 0.01	TTFT
ULAS 0034-0052	18.5	68.7 ± 1.4	583 ± 75	18.49 ± 0.04	TTKT
2MASS 0036+1821	4.0	114.417 ± 0.209	1869 ± 64	11.59 ± 0.03	TTFT
Gl 27B (0039+2115)	18.0	89.789 ± 0.058	793 ± 35	16.72 ± 0.03	TTFT
2MASS 0050-3322	17.0	94.6 ± 2.4	836 ± 71	16.04 ± 0.10	TTFT

Notes.
[a] For objects also listed in Table A1, the abbreviated name is given; full designations can be found in Table A1 itself. For all other objects, the full name is presented.
[b] This is the (near-infrared) spectral type, encoded as follows: M5 = −5.0, L0 = 0.0, L5 = 5.0, T0 = 10.0, T5 = 15.0, Y0 = 20.0, etc.
[c] This is a four-character code that gives the reference for the spectral type, parallax, effective temperature, and H-band magnitude, respectively: C = Gelino et al. (2011), D = Dupuy et al. (2015), F = Filippazzo et al. (2015), G = Gaia Collaboration et al. (2018), J = Faherty et al. (2012), K = Kirkpatrick et al. (2019a), L = Liu et al. (2012), T = Table A1 in this paper, W = Weinberger et al. (2016), X = Faherty et al. (2009).

(This table is available in machine-readable form.)

paper to include new Gaia parallaxes and improved parallaxes from Spitzer. We have also updated the H-band values where more accurate photometry is now available from VHS or other follow-up surveys. Those results are given in Table 14. We have extended this list into the Y dwarf regime by including objects from Table 10 of Kirkpatrick et al. (2019a) whose effective temperatures were calculated from published values computed using forward and inverse modeling techniques.

These results are plotted in Figure 22, and the fitted relations are given in Table 13. The plot in panel (a) shows that, from early-L through mid-T ($10.5 < M_H < 15$ mag), each 150 K bin in $T_{\rm eff}$ corresponds to a fairly narrow range of M_H. However, at spectral types later than mid-T ($M_H > 15$ mag), each 150 K temperature bin encompasses a larger and larger range of M_H values. In panel (b), we see the well-known result that objects in the L/T transition between types of late-L to mid-T span a very narrow range in $T_{\rm eff}$. Outside of this spectral type range, there is a monotonic trend of decreasing temperature with later spectral type.

For the 525 individual objects in the 20 pc census, we have assigned values of $T_{\rm eff}$ as follows; these values can be found in column 10 of Table 11. For old field dwarfs of normal gravity, we take the measured values of $T_{\rm eff}$ from Filippazzo et al. (2015) if the object has a computed value there. Otherwise, we assign a $T_{\rm eff}$ value via the relation in Figure 22(a), using the object's measured M_H if an H-band magnitude exists and the parallax is known to better than 12.5%. If these conditions are not met, we use the spectral type contained in the *SpAd* column of Table A1 along with the relation shown in Figure 22(b). The only exception is WISE 0855−0714, which is assigned a 250 K value, as was done in Kirkpatrick et al. (2019a).

For low-gravity (young) objects, we take the $T_{\rm eff}$ value computed by Faherty et al. (2016) if the object has a value there; otherwise, we take the value from Filippazzo et al. (2015). For other objects noted as young in column 11 of Table A1 but lacking measured values, we assign temperatures using an updated version (J. K. Faherty 2020, private communication) of the optical spectral type to $T_{\rm eff}$ relation of Faherty et al. (2016). When no optical type is available, we use the near-infrared type as a proxy.

For low-metallicity (subdwarf) objects, we take $T_{\rm eff}$ measurements directly from Filippazzo et al. (2015), when available. However, no relation between absolute magnitude (or spectral type) and temperature exists for these subdwarfs. Three mild, and presumably single, subdwarfs in our sample have measurements in Filippazzo et al. (2015): 2MASS 0729 −3954 (752 ± 69 K), 2MASS 0937+2931 (881 ± 74 K), and ULAS 1416+1348 (656 ± 54 K). The field relation would suggest values of 749 K, 858 K, and 610 K for these same three objects, respectively, showing that values from the field relation are consistent with the actual measurements. In fact, the most extreme subdwarf in the 20 pc sample, WISE 2005 +5424, has a model fit temperature of 600–900 K (Mace et al. 2013b), which is also roughly consistent with the field estimate of 574 K. Thus, as was done for the old field objects above, we assign temperatures to the other subdwarfs using the field relations of Figure 22.

8.2. Space Densities versus T_{eff} and Spectral Type

To aid in comparison to our mass function simulations, we present our final space densities as a function of temperature. Specifically, these are shown as histograms binned in 150 K-wide increments of $T_{\rm eff}$. To ease other empirical comparisons, we also present space densities as a function of spectral type, binned via integral subtypes.

Before computing these space densities, we must first determine whether the data contributing to each of these bins is complete to our target distance of 20 pc. For this, we use the $V/V_{\rm max}$ test advocated by Schmidt (1968). The basis of this test is as follows. Consider a proposed completeness limit of $d_{\rm max}$. For each object i at distance d_i within that distance, the test computes the ratio of the volume interior to that object's position, $V_i = (4/3)\pi {d_i}^3$, to the total volume being considered, $V_{\rm max} = (4/3)\pi {d_{\rm max}}^3$. The average of these ratios, $\langle V/V_{\rm max}\rangle = (1/n) \times \sum_{i=0}^{n}(V_i/V_{\rm max})$, should be ∼0.5 for a complete, isotropically distributed sample. Values that fall significantly below 0.5 indicate that there is incompleteness in the outer parts of the volume being considered. In other words, if the outer half-volume has significantly less than half of all

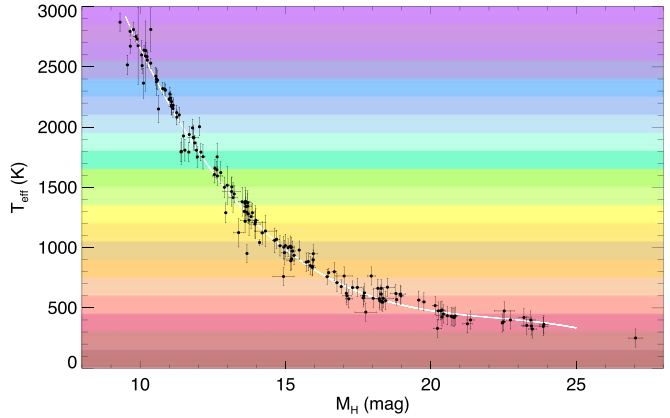

(a)

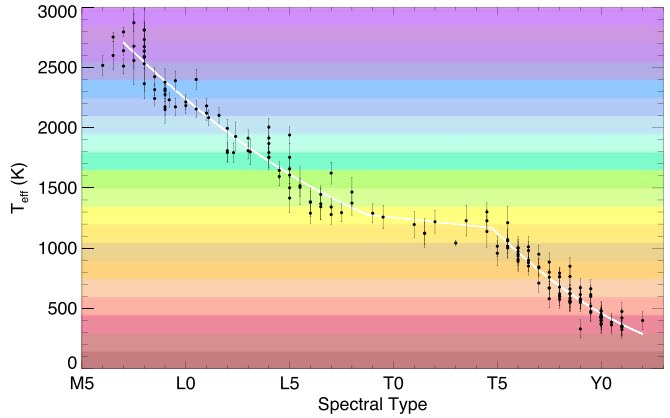

(b)

Figure 22. Plots showing the trend of absolute *H*-band magnitude with effective temperature (a) and spectral type with effective temperature (b), using the data (black points) from Table 14. Functional fits to the trends, shown by the white curves, can be found in Table 13. The colored bands in each plot depict each of the 150 K-wide temperature bins into which the data will be sorted in the following section.

objects within the total volume, the sample is likely incomplete to that distance.

We compute $\langle V/V_{\rm max}\rangle$ at half-parsec steps within each bin. The computation starts with the first half-parsec step falling just beyond the distance of the closest object in the bin and continuing out to $d = 20$ pc. These computations are graphically illustrated in Figure 23 for each bin in $T_{\rm eff}$ and in Figure 24 for each bin in spectral type. Practically, though, what does "significantly below 0.5" mean for $\langle V/V_{\rm max}\rangle$? Kirkpatrick et al. (2019a) proposed two ways to address this. First, a Poisson formalism was developed that establishes a 68% likelihood threshold (the equivalent of 1σ for a continuous distribution) that the $\langle V/V_{\rm max}\rangle$ is significantly different from 0.5, given the number of objects in the sample. These thresholds are shown as the light gray error bounds in Figures 23 and 24. Second, a run of 10,000 Monte Carlo simulations for a sample size of n objects was used to identify the range of $\langle V/V_{\rm max}\rangle$ around 0.5 that contains 68% of all simulated outcomes. Here, n is the number of objects in the most distant bin for which the Poisson formalism determined the sample to be complete. These simulated likelihoods are shown by the brown error bounds in the figures.

Using these methods, we find that our sample is likely complete[54] to 20 pc for all bins between 600 and 2250 K in $T_{\rm eff}$. For cooler bins, the completeness limit drops to 15 pc for 450–600 K and to 11 pc for 300–450 K. (The coolest bin with data, 150–300 K, has only one object in it, WISE 0855−0714, so the completeness cannot be computed.) We note, however, that the 300–450 K bin is likely complete over only a fraction of its 150 K interval, because the coldest assigned $T_{\rm eff}$ for any object in this bin is 367 K. We further note that two sources within the 525-object L, T, and Y dwarf 20 pc census—G 239-25B (1442+6603) and LSPM J1735+2634B—have assigned $T_{\rm eff}$ values (Table 11) that are hotter than the hottest temperature bin considered here. Finally, our measured space density in the 2100–2250 K bin should also be considered as a lower limit, because if we were to have included late-M dwarfs in our 20 pc census, some fraction of them would have populated this bin. These results are shown in the first three columns of the upper portion of Table 15.

Bins of integral spectral subtype, which generally have poorer statistics can, by extension, be assumed complete out to 20 pc for types warmer than 600 K, which is roughly late-T (Figure 22(b)). A close look at Figure 24 shows that the census appears to be complete for spectral types from L0 through T7.5. The completeness limit drops to ∼17 pc for types T8-T9.5 and to ∼13 pc for types Y0-Y1.5. Later types than this have only one representative per bin—WISE 1828+2650 at Y2 and WISE 0855−0714 at a type presumably later than that—so completeness limits cannot yet be determined. Results are shown in the first three columns of the lower portion of Table 15.

The bins in our $T_{\rm eff}$ and spectral type histograms are fixed, but our confidence in placing an object in a particular bin is directly related to the uncertainties in these quantities. For example, some of our objects have errors on $T_{\rm eff}$ that are comparable to our 150 K bin size, and the errors on some of our spectral types are also comparable to the integral spectral type bin size used. The lack of precision in these values is our greatest uncertainty in fixing the space densities in each bin. To address what the size of this uncertainty should be, we have run 10,000 Monte Carlo simulations for both the $T_{\rm eff}$ and spectral type distributions. For $T_{\rm eff}$, we have taken the error bars listed in Table 11, which were taken either from literature values (see Table 14) or assigned via the root-mean-square scatter from whichever relation in Table 13 was used for the $T_{\rm eff}$ estimate. For spectral type, we have assigned the standard 0.5-subclass uncertainty to all types except those with uncertainties already specified explicitly or for those with brackets or colons, for which we have assigned 1.0-subclass uncertainties. For each simulation, we take the $T_{\rm eff}$ or spectral type uncertainty and multiply it by a random value generated from a normal distribution having a mean of 0 and a standard deviation of 1. We add this uncertainty onto the measured value and then rebin. We then compute the means and standard deviations across all 10,000 simulations and report these in column 4 of Table 15.

These simulations do have a drawback, however, because the $T_{\rm eff}$ bins at either end of our 150–2250 K range are incomplete. First, the 1950–2100 K bin will contain objects that

[54] As explained later in this section, the 2100–2250 K bin is complete only for L dwarfs, but some late-M dwarfs are also expected to populate this temperature range. Hence, the space density derived for this bin should be considered a lower limit.

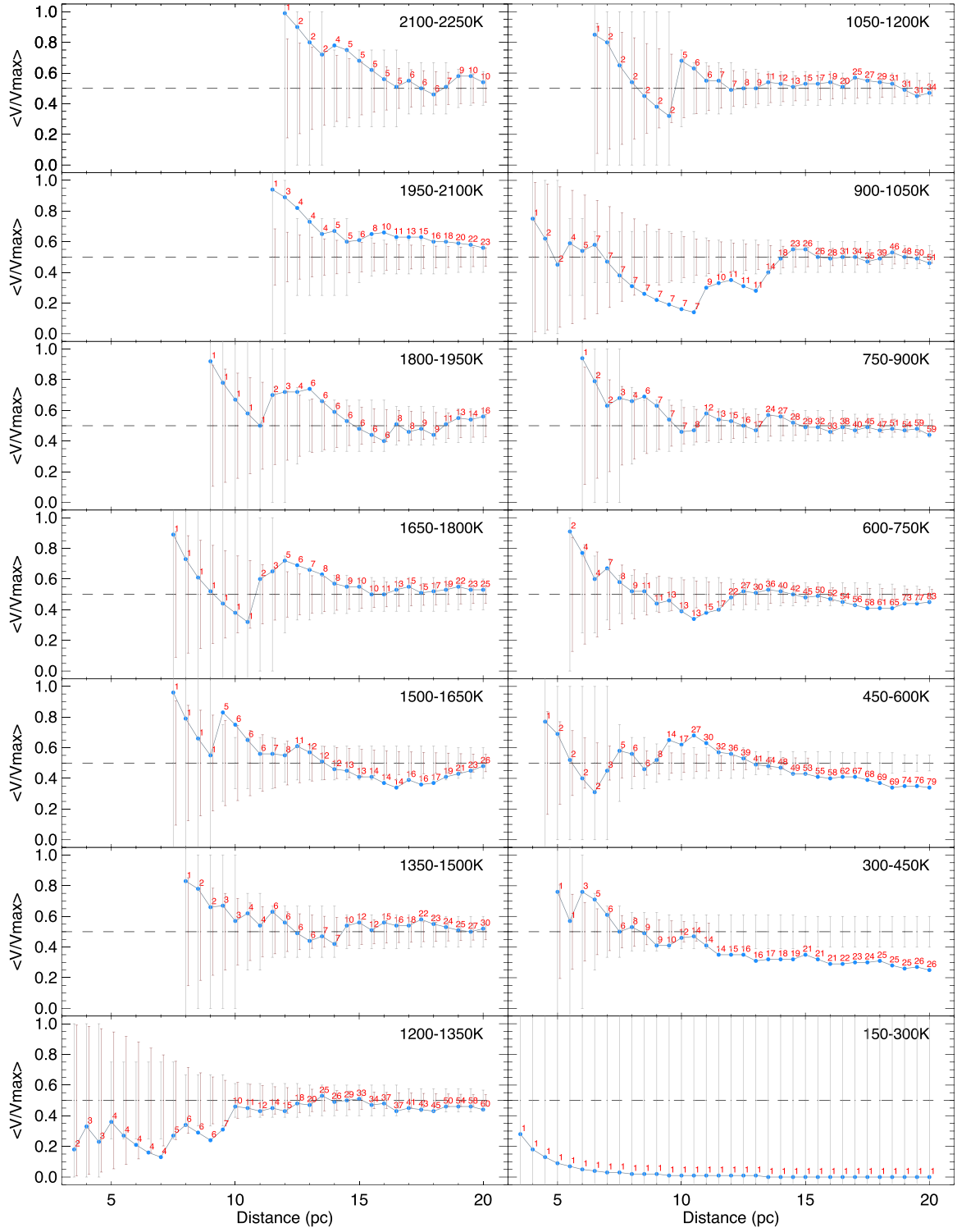

Figure 23. Average $V/V_{\rm max}$ value in 0.5 pc intervals for fourteen 150-K bins encompassing our 20 pc L, T, and Y dwarf census. Blue dots represent our empirical sample. Red labels mark the number of objects in the computation at each 0.5 pc interval. Black dashed line shows the $\langle V/V_{\rm max}\rangle = 0.5$ level indicating a complete sample. Gray error bars show the approximate 1σ range around $\langle V/V_{\rm max}\rangle = 0.5$ that a complete sample of the size indicated by the red number would exhibit, given random statistics. Brown error bars, offset by +0.05 pc from the gray error bars for clarity, show the 1σ variation around 0.5 obtained by 10,000 Monte Carlo simulations having the number of objects and completeness limit listed in Table 15.

scatter into the 2100–2250 K bin, but this loss in the cooler bin will not be mitigated by a concomitant gain from the warmer bin, because the object count in that latter bin is incomplete. Second, over the 300–750 K range, we encounter differing completeness limits in distance across the three bins that span this range as well as having an incompleteness in temperature in the 300–450 K bin. For example, objects that scatter from the 600–750 K bin into the 450–600 K bin will be lost if they have a distance larger than the completeness limit of that colder bin. Objects scattering in the other direction will not be similarly lost. The same is true of objects scattering between the 450–600 K bin and the 300–450 K bin. Given these biases, we

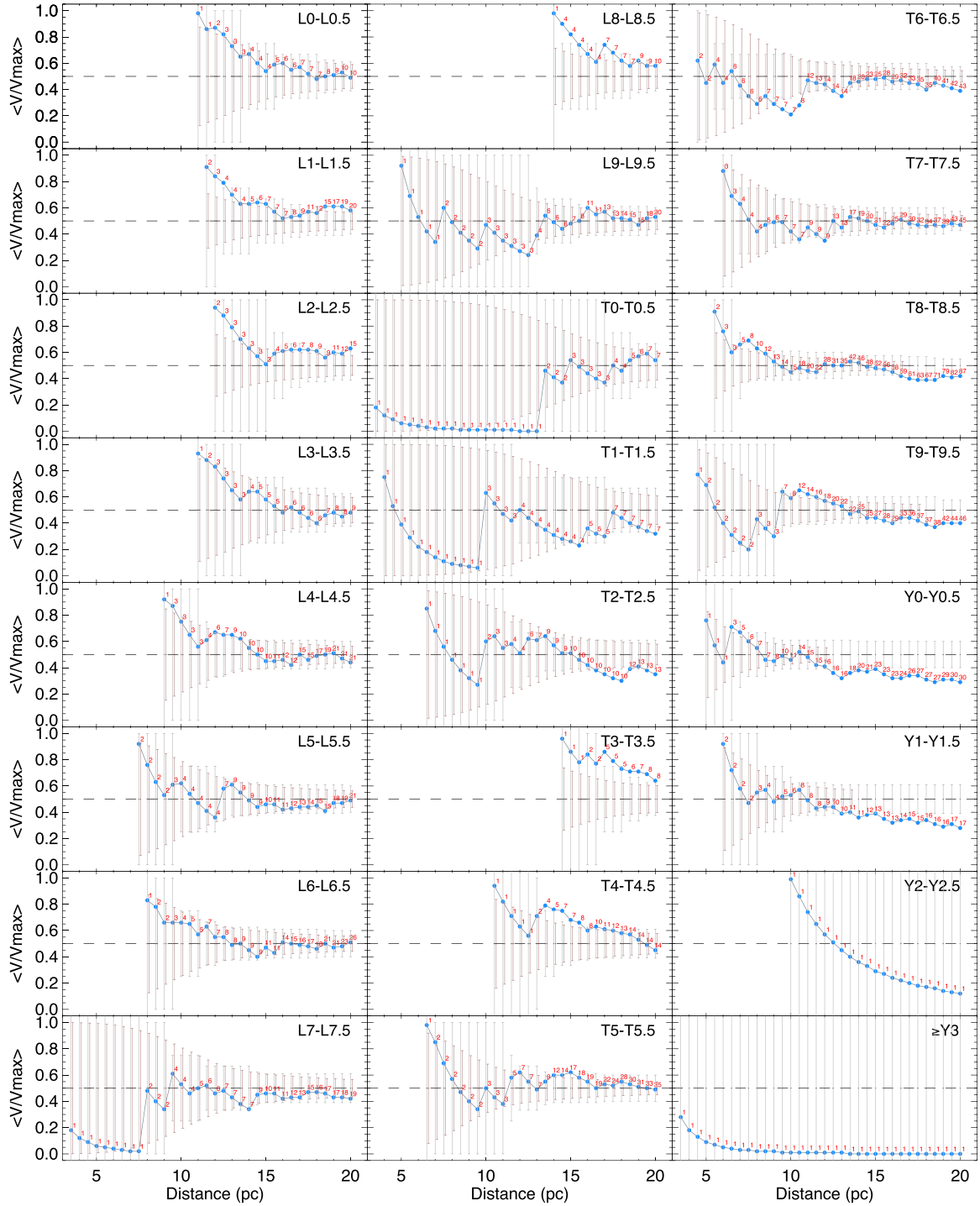

Figure 24. Average $V/V_{\rm max}$ value in 0.5 pc intervals for 24 integral spectral type bins encompassing our 20 pc L, T, and Y dwarf census. See the caption of Figure 23 for more details.

adopt a methodology whereby we use the raw number counts in each bin to set the space density, but we use the uncertainties from the simulations to set a conservative limit on their 1σ errors.

Although most of our bins pass the $\langle V/V_{\rm max}\rangle$ completeness test to 20 pc, this does not address whether there are inhomogeneities in the all-sky distribution. Kirkpatrick et al. (2019a) found an inhomogeneity in the T and Y dwarf counts toward the Galactic Plane, in which source confusion limits our ability to select objects in the faintest, coldest bins. We reinvestigate this here. Plots of our all-sky distributions broken down by broad spectral class are shown in Figures 25 and 26. The plot of T dwarfs appears to show a thinner area of coverage around and just south of the Galactic Plane in Figure 26(c).

We address this further by dividing objects in our 20 pc census into two sectors, one for the objects having an absolute Galactic latitude ($|{\rm glat}|) < 14\overset{\circ}{.}48$ (the "Plane" sector) and the second for objects having $|{\rm glat}| \geqslant 14\overset{\circ}{.}48$. This cut on |glat| was selected so that the first sector covers one quarter of the sky and the second covers the other three quarters. For each temperature

Table 15
Space Densities for Early-L through Early-Y Dwarfs

$T_{\rm eff}$ or SpT Bin[a] (1)	Complete-ness Limit (pc) $d_{\rm max}$ (2)	Raw No. of Objects *raw* (3)	Adjusted No. of Objects *adj* (4)	Corr. Factor *corr* (5)	Adopted Space Density[b] ($\times 10^{-3}$ pc^{-3}) *dens* (6)
2100–2250 K	20.0[c]	10	10.9 ± 2.5	1.05	>0.31
1950–2100 K	20.0	23	19.3 ± 3.2	1.05	0.72 ± 0.18
1800–1950 K	20.0	16	21.2 ± 3.6	1.05	0.50 ± 0.17
1650–1800 K	20.0	25	24.0 ± 3.8	1.05	0.78 ± 0.20
1500–1650 K	20.0	26	24.7 ± 3.9	1.05	0.81 ± 0.20
1350–1500 K	20.0	30	32.2 ± 4.5	1.05	0.94 ± 0.22
1200–1350 K	20.0	60	50.9 ± 5.2	1.09	1.95 ± 0.30
1050–1200 K	20.0	34	44.0 ± 5.2	1.09	1.11 ± 0.25
900–1050 K	20.0	51	48.6 ± 5.2	1.13	1.72 ± 0.30
750–900 K	20.0	59	58.4 ± 5.8	1.13	1.99 ± 0.32
600–750 K	20.0	83	76.0 ± 6.3	1.13	2.80 ± 0.37
450–600 K	15.0	53	44.9 ± 4.9	1.13	4.24 ± 0.70
300–450 K	11.0	14	16.7 ± 3.0	1.13	>2.84
150–300 K	…	1	…	…	…
L0–L0.5	20.0	10	8.1 ± 0.8	1.05	0.31 ± 0.10
L1–L1.5	20.0	20	21.7 ± 0.9	1.05	0.63 ± 0.14
L2–L2.5	20.0	15	13.7 ± 1.0	1.05	0.47 ± 0.13
L3–L3.5	20.0	9	9.6 ± 1.1	1.05	0.28 ± 0.10
L4–L4.5	20.0	21	20.5 ± 0.9	1.05	0.66 ± 0.15
L5–L5.5	20.0	21	21.8 ± 0.9	1.05	0.66 ± 0.15
L6–L6.5	20.0	26	22.6 ± 1.4	1.05	0.81 ± 0.17
L7–L7.5	20.0	19	21.6 ± 1.5	1.05	0.60 ± 0.14
L8–L8.5	20.0	10	11.2 ± 0.8	1.05	0.31 ± 0.10
L9–L9.5	20.0	20	19.5 ± 0.5	1.05	0.63 ± 0.14
T0–T0.5	20.0	7	7.0 ± 0.7	1.13	0.24 ± 0.09
T1–T1.5	20.0	7	7.5 ± 0.5	1.13	0.24 ± 0.09
T2–T2.5	20.0	13	13.0 ± 0.1	1.13	0.44 ± 0.12
T3–T3.5	20.0	8	7.0 ± 0.7	1.13	0.27 ± 0.10
T4–T4.5	20.0	14	14.5 ± 0.9	1.13	0.47 ± 0.13
T5–T5.5	20.0	35	34.5 ± 0.9	1.13	1.18 ± 0.20
T6–T6.5	20.0	43	43.5 ± 1.0	1.13	1.45 ± 0.22
T7–T7.5	20.0	45	43.5 ± 1.2	1.13	1.52 ± 0.23
T8–T8.5	16.5	59	58.0 ± 1.5	1.13	3.54 ± 0.47
T9–T9.5	17.5	37	37.0 ± 1.8	1.13	1.86 ± 0.32
Y0–Y0.5	12.0	16	17.0 ± 0.7	1.13	2.50 ± 0.63
Y1–Y1.5	13.5	11	10.0 ± 1.0	1.13	1.21 ± 0.36
Y2–Y2.5	…	1	…	…	…
⩾Y3	…	1	…	…	…

Notes.
[a] The *SpAd* spectral type from Table A1, which defaults to near-infrared types, is used here.
[b] This value is computed via the equations

$$\text{dens} = (\text{raw})(\text{corr})/\left(\frac{4}{3}\pi {d_{\rm max}}^3\right)$$

and

$$\sigma_{\rm dens} = \sqrt{({\sigma_{\rm raw}}^2 + {\sigma_{\rm adj}}^2)}(\text{corr})/\left(\frac{4}{3}\pi {d_{\rm max}}^3\right),$$

where $\sigma_{\rm raw} = \sqrt{\rm raw}$.
[c] This bin is complete only for its L dwarf complement. Since late-M dwarfs are also expected to populate this bin, the derived space density is considered to be a lower limit.

and spectral type bin, we can therefore determine if the numbers in the Plane sector, when tripled, appear to be significantly lower than those found in the second sector. Using the complete samples as defined in Table 15, we find 27 Y0-Y1.5 dwarfs. Of these, 23 lie outside of the Plane sector, meaning that we would expect $23/3 \approx 8$ similar objects to lie in the Plane sector itself. However, only four are found there, for a shortfall of four—or 15% of the total sample. Using the same methodology and combining spectral bins to increase the statistical significance of each binned population, we find shortfalls of 13% for T8-T9.5 (96 objects total), 10% for T6-T7.5 (88 objects total), 14% for T4-T5.5 (49 objects total), 12% for T0-T3.5 (35 objects total), 5% for L6-L9.5 (75 objects total), and 5% for L0-L5.5 (96 objects total). We thus apply an

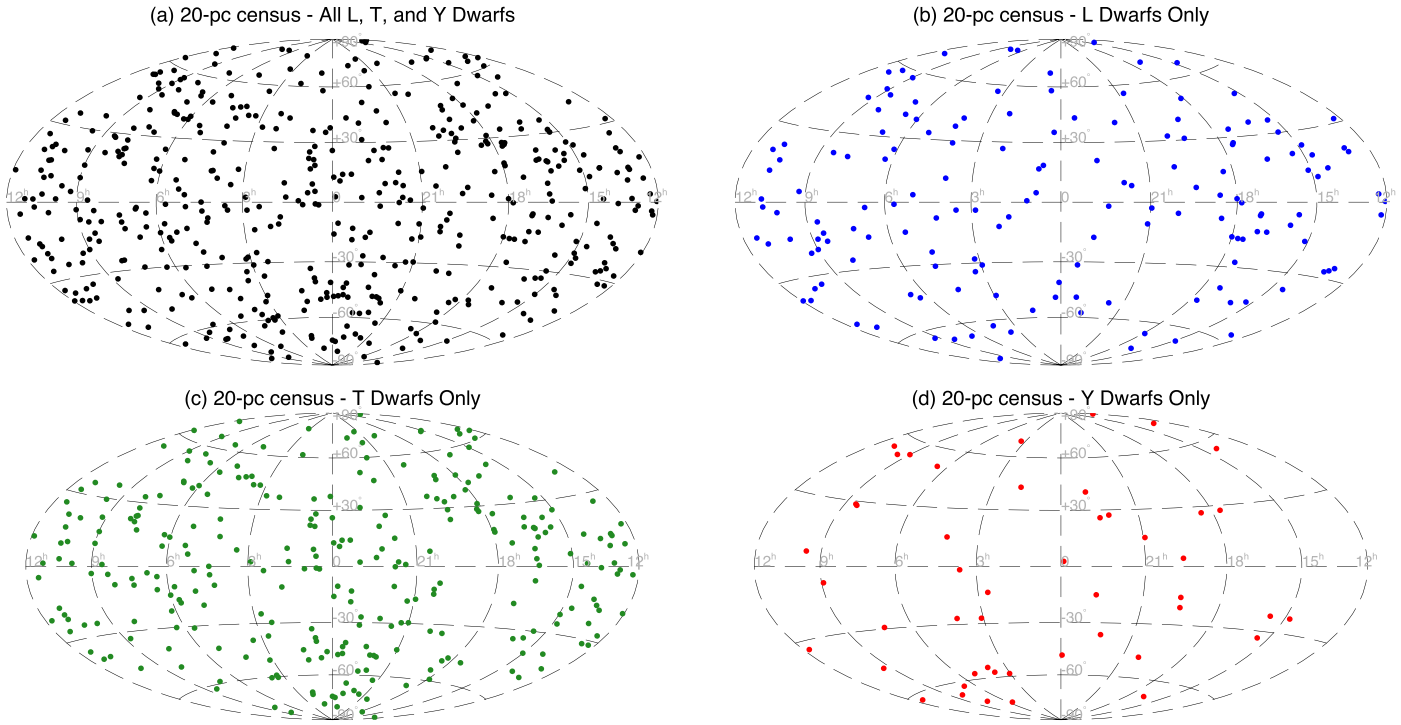

Figure 25. Plots of the 20 pc L, T, and Y dwarf sample in equatorial coordinates. The four panels display the sample in its entirety (black), only the L dwarfs (blue), only the T dwarfs (green), and only the Y dwarfs (red).

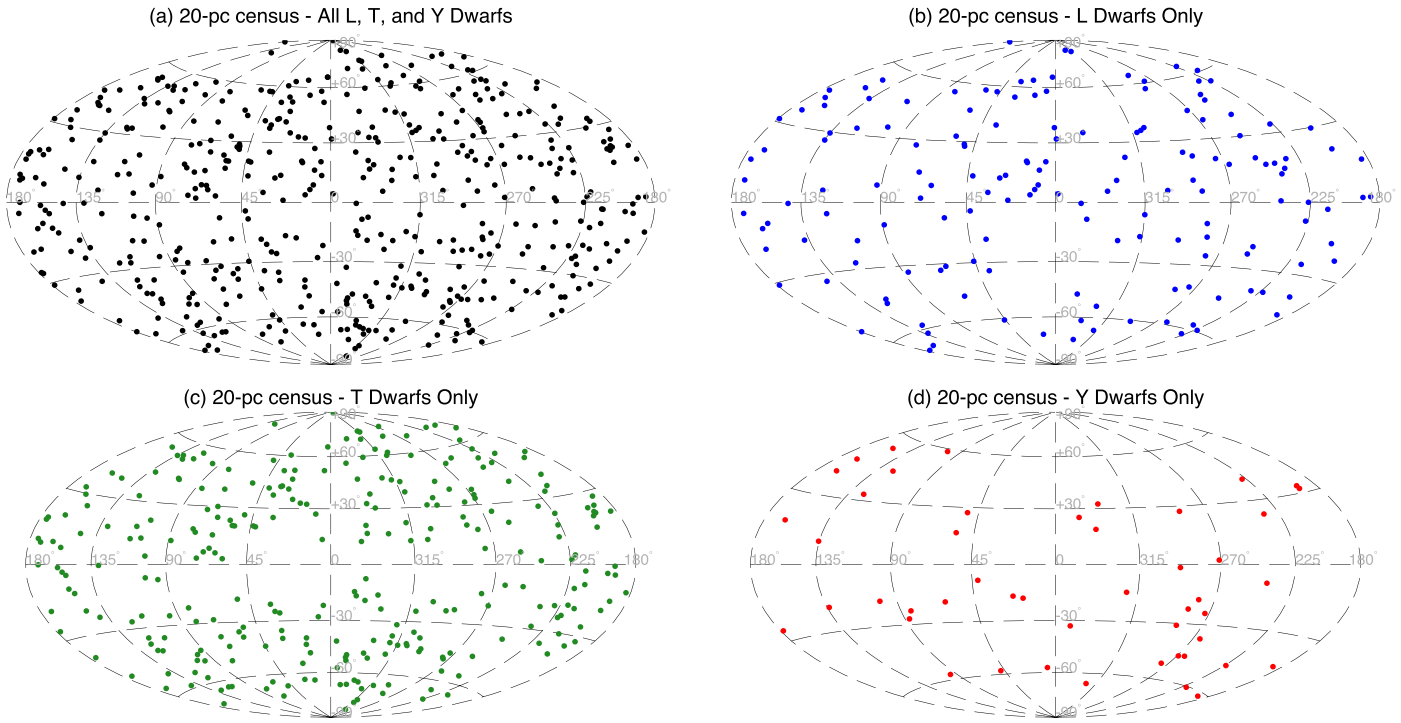

Figure 26. Plots of the 20 pc L, T, and Y dwarf sample in Galactic coordinates. See the caption to Figure 25 for more details.

adjustment factor of 1.05 across the L dwarf densities and 1.13 across the T and Y dwarf densities. We apply these same factors to the $T_{\rm eff}$-based densities, and use an average adjustment factor of 1.09 to the 1050–1350 K bins that cross the L/T transition. These factors are listed in the fourth column of Table 15. To compute the space densities, we used the formulae given in the footnotes of Table 15. These final values are given in column 6 and are represented graphically in Figure 27.

We can compare these results to other recent determinations in the literature. At early-L types, Bardalez Gagliuffi et al. (2019) find space densities of $[0.75 \pm 0.13,\ 1.02 \pm 0.16,\ 0.78 \pm 0.14,\ 0.58 \pm 0.12,\ 0.88 \pm 0.15,\ 1.44 \pm 0.19] \times 10^{-3}$ pc^{-3} per integral spectral type bins of [L0–L0.5, L1–L1.5, L2–L2.5, L3–L3.5,

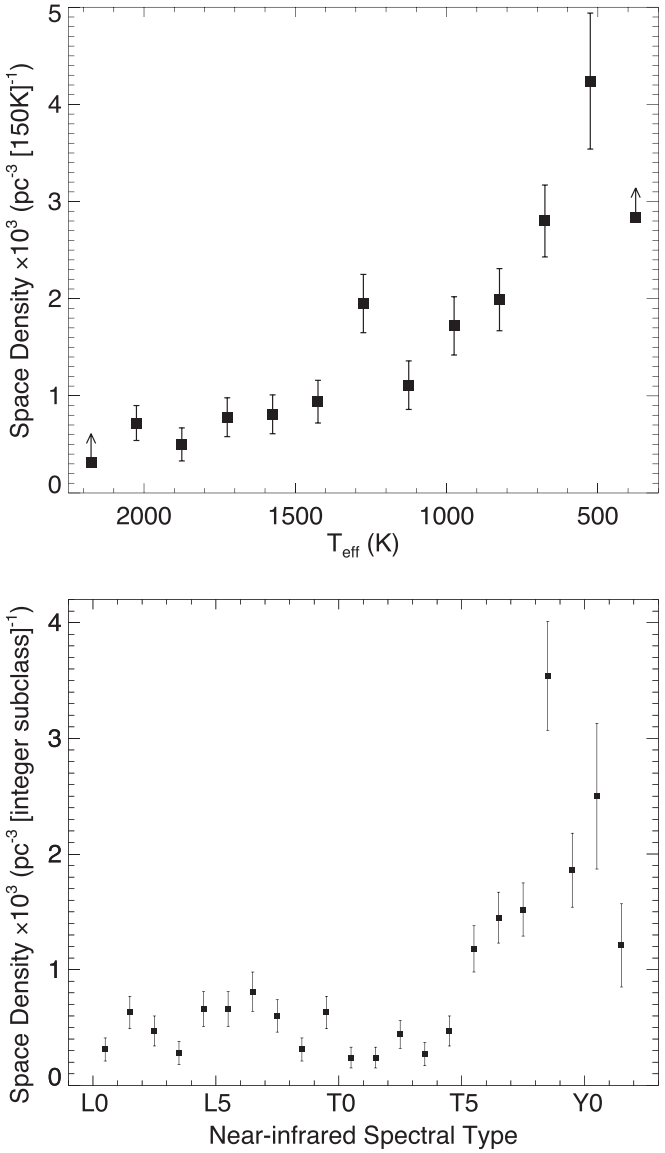

Figure 27. Our measured space densities from Table 15. (Top) Space densities as a function of effective temperature. (Bottom) Space densities as a function of near-infrared spectral type.

L4–L4.5, L5–L5.5]. Our space density determinations across each of these bins differ by an average of 2.1σ, and the Bardalez Gagliuffi et al. (2019) results are consistently a factor of ∼1.9 higher. However, D. C. Bardalez Gagliuffi (2020, private communication) has found that their published densities included a pessimistic set of assumptions in their completeness calculation. Our Table 15 values compare favorably to the $T_{\rm eff}$-binned values of Kirkpatrick et al. (2019a), the greatest deviations being a 1.2σ variation (difference factor of 0.84 between Kirkpatrick et al. (2019a) and this paper) in the 750–900 K bin and a 1.4σ variation in the opposite direction (difference factor of 1.27) in the adjacent 600–750 K bin.

9. Determining the Mass Function

In Kirkpatrick et al. (2019a), we developed a formalism for translating various forms of the mass function into the observational domain, since mass is not an observable quantity for most objects within the 20 pc census. There are several steps in doing this, which we summarize below.

First, we considered a variety of functional forms of the mass function that have been proposed in the literature. These include power laws ($dN/dM \propto M^{-\alpha}$) with α values ranging from −1.0 to 1.5, the log-normal distribution ($dN/dM \propto e^{-(\ln(M)-\mu)^2/2\sigma^2}$) with values of the mean (μ) and standard deviation (σ) taken from Chabrier (2001, 2003b) and Chabrier (2003a), and a bipartite power law favored by Kroupa et al. (2013). These forms determine the distribution of masses produced.

Second, a stellar birthrate that has remained constant in time over the past 10 Gyr was assumed. Burgasser (2004) found that the stellar luminosity function for T dwarfs is largely invariant to the birthrate assumed, although the L dwarf regime can still bear an imprint from recent events if star formation is more episodic. Allen et al. (2005) explored this further and found that changes in the luminosity function produced by the underlying mass function were much larger than those produced by variations in the birthrate.

Third, because most of the objects in our simulations are brown dwarfs, the observable quantity we use for the empirical determinations ($T_{\rm eff}$) changes with time as the brown dwarf ages and cools. Hence, we tie each simulated object to an evolutionary path applicable to its mass, so that we can determine its current $T_{\rm eff}$. Two sets of evolutionary models were employed for this, resulting in two different sets of simulated $T_{\rm eff}$ distributions. The first were the solar-metallicity COND models from Baraffe et al. (2003) that, because they neglect dust opacity, are most applicable to mid-M dwarfs and mid- to late-T dwarfs believed to be free of photospheric clouds. These model grids are sampled at five different ages (0.1, 0.5, 1, 5, and 10 Gyr) and sample the temperature range 125 K $\lesssim T_{\rm eff} \lesssim$ 2800 K, which corresponds to masses around $0.01M_{\odot} < M < 0.10M_{\odot}$. The second set of models were the hybrid suite of solar-metallicity models from Saumon & Marley (2008) that assume cloud-free atmospheres only in the late-M and late-T zones but account for cloud growth and subsequent clearing in and around the transition from L dwarfs to T dwarfs. The evolutionary model grids are sampled at 26 different ages in the 3 Myr < age < 10 Gyr range and cover the range 300 K $\lesssim T_{\rm eff} \lesssim$ 2400 K, which corresponds to the mass range $0.002M_{\odot} < M < 0.085M_{\odot}$.

Fourth, we used the inverse transform sampling method to turn the various forms of the mass function into space densities binned in $T_{\rm eff}$. The process is as follows. Each normalized mass function can be used as a probability density function, which gives the likelihood of drawing at random an object of a certain mass from within that distribution. In a practical sense, this random drawing is done by integrating under the probability density function to produce a cumulative distribution function, reversing the dependent and independent variables, and re-solving for the dependent variable, thus creating the inverse cumulative distribution function that then provides a mapping from a random seed to an actual mass. The seed is produced via a random sampling of a uniform distribution over the range zero to one.

Fifth, we performed the simulations by creating 3×10^6 random seeds, each of which was assigned an age according to its order of selection. These ages were distributed uniformly over the subset of 0–10 Gyr interval over which each evolutionary model is valid. The seed was then passed through the inverse cumulative distribution function to assign its mass, then the assigned age and mass were passed through the

evolutionary models to get the current $T_{\rm eff}$. Because the evolutionary models are sampled only on a sparse grid, bilinear interpolation between neighboring points was used to assign the temperature.

Finally, simulations were produced for each of the 12 assumed functional forms of the mass function, each of which was run through the two different evolutionary model grids. Furthermore, each simulation was run with three different values of a cutoff mass ($10M_{\rm Jup}$, $5M_{\rm Jup}$, or $1M_{\rm Jup}$,), which is the lowest mass product that can be created. This resulted in a grid of 72 simulated $T_{\rm eff}$ distributions.

9.1. Mass Function Fits

Here, we compare our measured space densities to these 72 simulations. To determine the simulation that fits best, we have used the IDL routine `mpfit` (Markwardt 2009) to perform a weighted least-squares fit between the data and the simulations, where the only adjustable parameter is the scaling between the arbitrary number counts in the models and our measured space densities. For the calculation, we use only the 11 values in the upper portion of Table 15 that cover the range 450–2100 K, as the other values are lower limits only. The best fit to each model produces a reduced χ^2 value.

Figure 28 shows the fits for which this value is minimized. These best fits are identical to the best fits found by Kirkpatrick et al. (2019a), and involved the single power-law and log-normal forms. For each evolutionary model, the power-law form is slightly favored over the log-normal based on the best-fit χ^2 minimization values. In contrast to the results of Kirkpatrick et al. (2019a), we now find that the evolutionary code of Saumon & Marley (2008) is highly favored over that of Baraffe et al. (2003), and the reason for this is the inclusion in this paper of space density measurements over the cloudy-to-clear transition that the Saumon & Marley (2008) models were designed to address. Specifically, the space density spike in the 1200–1350 K bin of Figure 28 is well-produced by simulations incorporating the Saumon & Marley (2008) models, and this bin is the one covering spectral types from ∼L8 to ∼T3 (the yellow zone in Figure 22(b)) over which cloud building and subsequent breakup have been hypothesized. These models not only predict the position of the spike but also correctly predict its magnitude. Furthermore, they also predict the magnitude of the drop-off and recovery at cooler types once clouds have cleared and cooling once again proceeds as normal.

The best fits across the coarse grid of 72 models are those with the single power law of $\alpha = 0.5$. Figure 29 illustrates a few supplemental simulations to show that the minimum χ^2 value across a finer grid of models is actually reached at $\alpha = 0.6$, which was the same conclusion found by Kirkpatrick et al. (2019a). There is, however, no significant difference between the χ^2 values of the $\alpha = 0.5$, 0.6, and 0.7 models. Obtaining a more accurate space density in the 450–600 K bin is critical to pinning down the true value of α.

As a closer look at Figure 29 reveals, the preferred value of α rests largely with the steepness of the curve over the 1200–450 K region, and most of the power falls in that region's final bin (450–600 K), for which the space density is the highest. If we use the densities implied by our temperature randomizations (column 4 of Table 15), we find a best fit of $\alpha = 0.4$, although, as discussed earlier, the density for that bin is likely biased low. This leads us to conclude that our measurements of the space density support a value of $\alpha = 0.6 \pm 0.1$.

9.2. The Low-mass Cutoff

Whereas the 450–600 K bin is critical in determining the value of the power law's exponent, the next cooler bins are critical in determining the cutoff mass. The best fits to our observed space densities currently do not have a strong dependence on the low-mass cutoff. As the plots in Figure 29 show, this is because the lower limit to the density in the 300–450 K bin is consistent with all three values of the cutoff mass (10, 5, and 1 $M_{\rm Jup}$). An increase of just 40% in the value of this lower limit would enable us to confidently claim a cutoff mass below $10M_{\rm Jup}$. (In Kirkpatrick et al. (2019a), we claimed to push the cutoff mass below $5M_{\rm Jup}$, but this was based on a number of objects in the 300–450 K bin that was half as large as the sample we are now using.) This bin is comprised mostly of Y0.5 to Y2 dwarfs (Figure 22(b)), which are challenging objects to uncover, given their faint absolute magnitudes ($M_J \approx M_H > 23$ mag, $M_{\rm W2} = M_{\rm ch2} > 15$ mag; Figure 16).

Even more critical to defining the low-mass cutoff is the next cooler bin, 150–300 K, which presently has only one known object in it, WISE 0855−0714. Finding more representative objects in this bin would even more readily determine the cutoff mass, as the top row of Figure 28 shows. For the $\alpha = 0.5$ model, the space density values in this bin vary wildly—from $\sim 0.2 \times 10^{-3}$ pc^{-3} for a $10M_{\rm Jup}$ cutoff, to $\sim 2.2 \times 10^{-3}$ pc^{-3} for a $5M_{\rm Jup}$ cutoff, to $\sim 4.5 \times 10^{-3}$ pc^{-3} for a $1M_{\rm Jup}$ cutoff. Finding objects in this bin is an even more challenging proposition, as WISE 0855−0714 itself has absolute magnitudes of $M_J \approx 28$ mag, $M_H \approx 27$ mag, and $M_{\rm W2} = M_{\rm ch2} \approx 17$ mag.

Nonetheless, we can use objects of known mass within the 20 pc census to help further refine the cutoff value. Most notably, a number of census members are known to belong to young moving groups and associations (Section 7.1), and these objects will have hotter temperatures and earlier spectral types than older counterparts in the field of the same mass. Hence, finding an object of exceedingly low mass is a far less daunting challenge if it is younger and brighter. Young members of the 20 pc census are listed along with their assigned $T_{\rm eff}$ values and published masses in Table 16.

Before exploring these masses, though, we note that such determinations are direct comparisons to evolutionary models and thus fail to provide an independent check of the theory. Are the masses coming from the evolutionary models trustworthy? To answer this, we have also listed in Table 16 those multiple systems within the 20 pc census whose masses have been measured dynamically. These objects are identified with their corresponding $T_{\rm eff}$ bin and indicated in Figure 30. This figure shows, for both the Saumon & Marley (2008) and Baraffe et al. (2003) evolutionary tracks, the expected mass distributions from our simulations for each of our 150 K bins. The simulations show a tight distribution of masses for the hotter bins, but the range of masses quickly expands for the colder bins. In the Saumon & Marley (2008) models, a wide range of masses is expected to inhabit each of the temperature bins from 750 to 1500 K. At colder temperatures, though, the mass range reduces dramatically, with the 300–450 K bin containing only objects with masses below $\sim 30M_{\rm Jup}$. (Using the

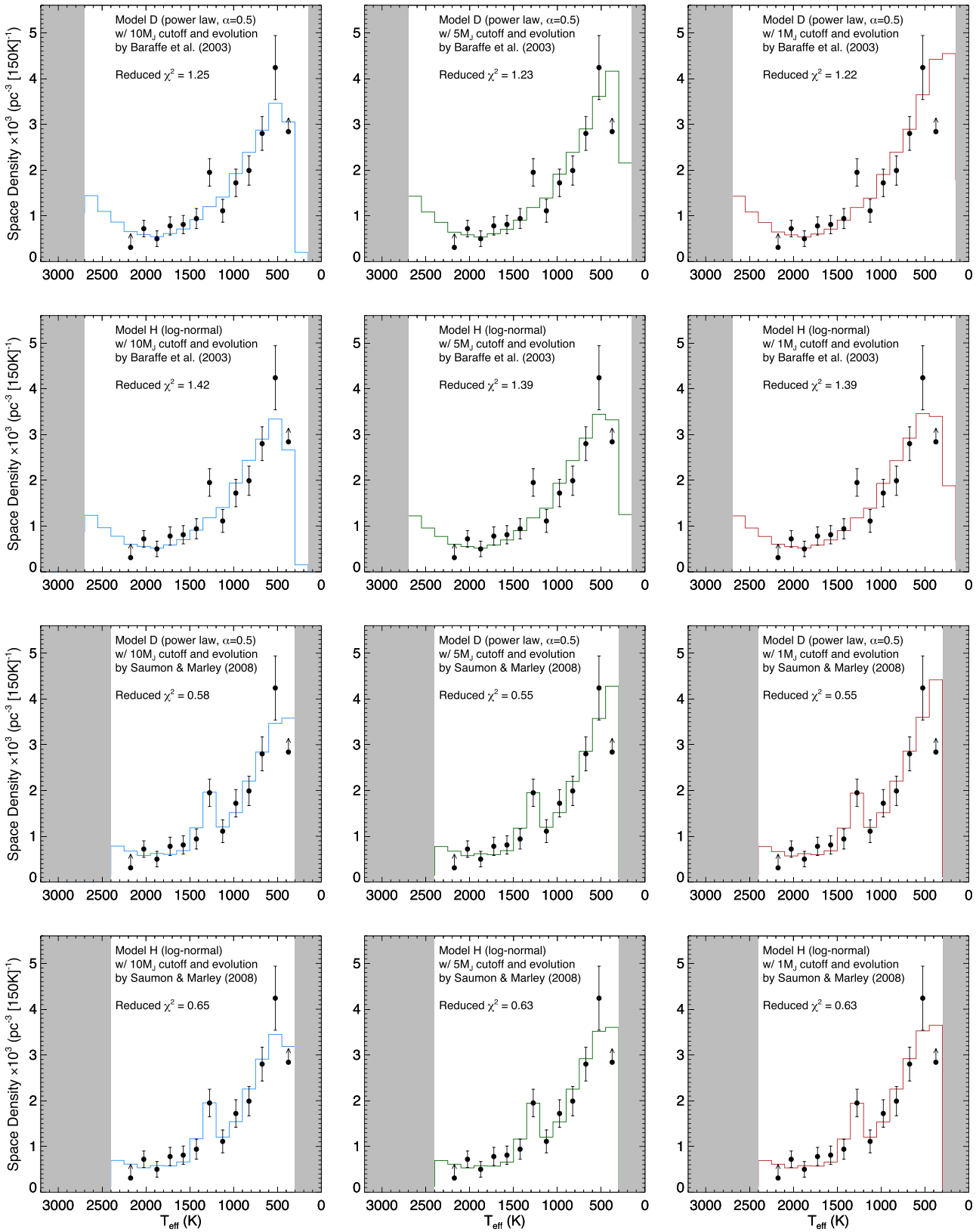

Figure 28. Best fits between the simulations and our measured space densities. Of the simulations that use the evolutionary tracks of Baraffe et al. (2003), the two with the smallest reduced χ^2 values are shown in the top two rows. Of the simulations that use the evolutionary tracks of Saumon & Marley (2008), the two that provide the best fits are show in the two bottom rows. "Model D" refers to the power law with $\alpha = 0.5$, and "Model H" refers to the single-object log-normal form of Chabrier (2001). See Kirkpatrick et al. (2019a) for additional information on these simulations. Each row shows the same model with a different low-mass cutoff: $10M_{\rm Jup}$ (blue) in the left panel, $5M_{\rm Jup}$ (dark green) in the middle panel, and $1M_{\rm Jup}$ (red) in the right panel. Our measured space densities and their uncertainties are shown in black. Gray zones denote areas not covered by the simulations.